ROYAL SOCIETY OF CHEMISTRY

PAPER

Check for updates

Effects of cation size on thermoelectricity of PEDOT:PSS/ionic liquid hybrid films for wearable thermoelectric generator application†

Kexing Jiang,‡[a] Shao-Huan Hong,‡[a] Shih-Huang Tung [b] and Cheng-Liang Liu [b] *[c]

The conjugated polymer PEDOT:PSS and the related hybrid systems undoubtedly possess a high electrical conductivity and a reasonable Seebeck coefficient, showing potential for thermoelectric applications due to the feasibility of modulating their degree of doping by partially extracting the PSS section. Herein, the combination of PEDOT:PSS, with four ionic liquids (XMIM BF$_4$) having cations of various alkyl chain lengths (methyl, ethyl, butyl, and hexyl denote X = M, E, B, and H, respectively) and the same tetrafluoroborate BF$_4$ anion, was studied to optimize the thermoelectricity. It was found that the introduction of ionic liquids with small-(MMIM BF$_4$) and large-sized cations (HMIM BF$_4$) into the PEDOT:PSS film contributes to an improved Seebeck coefficient and conductivity, respectively. The obtained PEDOT:PSS/MMIM BF$_4$ hybrids display a remarkably enhanced thermoelectric performance with the highest power factor of 86.3 μW m^{-1} K^{-2} measured at 313 K. The maximum output power of the robust 7-leg thermoelectric module reaches 10.4 nW for a temperature gradient of 14.0 K. It also exhibits excellent environmental stability with less than 10% variation in resistance for 28 days at room temperature without encapsulation and excellent mechanical flexibility under 500 bending cycles, respectively. A prototype wearable thermoelectric generator installed on the human wrist generates a thermovoltage of ~0.74 mV with a 4.3 K temperature difference relative to the colder surroundings. Our finding highlights the importance of the rational selection of ionic liquids for enhancing the thermoelectric properties of a PEDOT:PSS film and indicates its potential for use in power generators.

1. Introduction

Thermoelectric materials can play a crucial role in renewable energy technologies and provide a potential solution to solve global energy shortage problems. Recently, many studies have focused on high-temperature bulk thermoelectric materials,[1–5] such as chalcogenides, clathrates, intermetallic alloys, and skutterudites. However, conducting polymers, as an emerging class of thermoelectric materials, have recently carved out a special place in the field of thermoelectricity due to their intrinsic flexibility, cost effectiveness, and low thermal conductivity.[6–16] Although these conducting polymer-based materials cannot substitute conventional inorganic materials at higher temperatures in terms of efficiency and stability, their

non-toxicity, environmental friendliness, and solution processability enable them to overshadow their inorganic counterparts in low-temperature waste heat recovery. Moreover, the diverse morphologies and structures of the conducting polymers can be easily tuned through many approaches, such as chain alignment, nanostructuring, and doping, to manipulate their charge transport as well as thermoelectric characteristics.[17–24]

Within these conjugated polymer systems, poly(3,4-ethylenedioxythiophene):poly(styrene sulfonate) (PEDOT:PSS), with its enhanced solubility from the aqueous dispersion of soluble polymeric counterions, has gained attention as a state-of-the-art thermoelectric polymer and is currently the best-performing conjugated polymer.[25–31] To date, strategies that can improve the overall thermoelectric properties of a PEDOT:PSS film determined by using the power factor have been studied. Because the degree of doping of a conjugated polymer influences the Seebeck coefficient and conductivity,[25] the dilemma of these two thermoelectric parameters should be considered. This doping level can be controlled *via* the secondary doping process by blending PEDOT:PSS with a secondary dopant in an aqueous suspension or post-treatment of coated PEDOT:PSS films.[26,27] The chemicals for secondary dopants can be polar organic solvents,[32,33] such as dimethylsulfoxide (DMSO) and

[a]Department of Chemical and Materials Engineering, National Central University, Taoyuan 32001, Taiwan

[b]Institute of Polymer Science and Engineering, National Taiwan University, Taipei 10617, Taiwan

[c]Department of Materials Science and Engineering, National Taiwan University, Taipei 10617, Taiwan. E-mail: liucl@ntu.edu.tw

† Electronic supplementary information (ESI) available. See https://doi.org/10.1039/d2ta05134f

‡ These authors contributed equally to this work.

ethylene glycol (EG); inorganic salts;[34] and various organic carboxylic and inorganic acids,[33,35] such as formic acid and sulfuric acid. Only one secondary dopant or several dopants in a combined form could be involved. The presence of a secondary dopant favors better polymer chain organization in morphologies and removes the excess insulating PSS segments; thus, the conductivity can be significantly enhanced by several orders of magnitude. Another effective strategy involving chemical (*via* reducing agent) and electrochemical dedoping of PEDOT:PSS films can be also applied for improving the thermoelectric properties.[36–38] The dedoping process aims to remove doped anions, which may reduce the charge carrier concentration of PEDOT:PSS, thereby resulting in an enhancement of the Seebeck coefficient. PEDOT:PSS/ionic liquid heterostructures were found to further enhance the thermoelectric properties.[39] Liu *et al.* first cast the PEDOT:PSS/BMIM BF$_4$ hybrid film for simultaneously improving the electrical conductivity and Seebeck coefficient up to 174 S cm^{-1} and 30 μV K^{-1}, respectively.[40] Later Kee *et al.* reported that ionic liquids consisting of EMIM DCA or EMIM DCl can manipulate the doping level and nanostructure of PEDOT:PSS through ion exchange, which leads to a remarkable increase in the conductivity and Seebeck coefficient (up to 538 S cm^{-1} and 35 μV K^{-1}, respectively).[41] Similar contributions have been realized for PEDOT:PSS films constructed by ionic liquid coatings based on BMIM or EMIM cations with various anions;[42–53] and their thermoelectric performances are summarized in Table S1.† The addition of or treatment with these ionic liquids in previous studies indicates the direction for manipulating the thermoelectric performance. However, to the best of our knowledge, the influence of cation sizes on the thermoelectric properties of PEDOT:PSS films has not been fully studied yet.[54,55] Besides, the development of wearable thermoelectric generators can address the conversion of thermal difference into useful electrical energy, which can harness waste or surrounding heat and emerge as a green tool for small-scale power generation. The unexplored mechanisms for achieving enhanced thermoelectricity and flexibility of PEDOT:PSS films modified with ionic liquids for thermoelectric generator modules should be investigated further.

In this work, we systematically investigate the effect of cationic species of ionic liquid additives on the thermoelectric performance of spin-coated PEDOT:PSS films by introducing four ionic liquids (XMIM BF$_4$) with cations having various alkyl chain lengths (from methyl to hexyl) and a BF$_4$ anion. It was revealed that the maximum enhancement in the Seebeck coefficient and conductivity is achieved for the PEDOT:PSS films incorporated with ionic liquids with a shorter and longer side chain length of cation, respectively. The mechanism by which these ionic liquids influence the resulting PEDOT:PSS/ionic liquids has been elucidated through absorption spectroscopy, Raman spectroscopy, X-ray photoelectron spectroscopy (XPS), and grazing incidence wide-angle X-ray scattering (GIWAXS). The drop-cast PEDOT:PSS post-treated with MMIM BF$_4$ and high-dielectric-constant formamide provide optimized thermoelectric properties with a conductivity of 1447.3 S cm^{-1}, a Seebeck coefficient of 24.4 μV K^{-1}, and a superior power factor of up to 86.3 μV m^{-1} K^{-2}. Finally, the thermoelectric modules

based on these ionic liquid-modified PEDOT:PSS films were demonstrated to have a maximum power of 10.4 nW. They were further assembled into a prototype of a wearable thermoelectric generator for collecting waste heat under the temperature gradient between the human wrist and ambient atmosphere as heating and cooling sources, respectively.

2. Experimental section

Preparation of ionic liquid-modulated PEDOT:PSS hybrid films

The aqueous PEDOT:PSS solution (Clevios PH1000; a concentration of 1.3 wt% and weight ratio of 1 : 2.5) was purchased from Heraeus and refrigerated at 4 °C. The ionic liquids including 1,3-dimethylimidazolium tetrafluoroborate (MMIM BF$_4$; 98%), 1-ethyl-3-methylimidazolium tetrafluoroborate (EMIM BF$_4$; >97%), 1-butyl-3-methylimidazolium tetrafluoroborate (BMIM BF$_4$; ≥97.0), and 1-hexyl-3-methylimidazolium tetrafluoroborate (HMIM BF$_4$; ≥97%) were supplied by Rhawn Reagent, Sigma-Aldrich, Alfa Aesar, and TCI, respectively. All chemicals were used as received without further purification. A different type of ionic liquid (MMIM BF$_4$, EMIM BF$_4$, BMIM BF$_4$, and HMIM BF$_4$) with varying amounts was added into the PEDOT:PSS solution; then, it was mixed vigorously using a vortex mixer for 5 min. The PEDOT:PSS/ionic liquid mixture dispersion was two-step spin-coated (first step: 1000 rpm for 10 s; second step: 2500 rpm for 30 s) onto a pre-cleaned glass substrate and annealed at 140 °C for 20 min in an ambient atmosphere. The post-treatment of the PEDOT:PSS/ionic liquid films was conducted by dropping 100 μL of DMSO onto the center of the film surface, spinning at 2000 rpm for 30 s, and finally drying at 140 °C for 10 min.

Free-standing films were obtained by the following three procedures: drop-casting, ionic liquid post-treatment, and falling off from the substrates. A pristine PEDOT:PSS film was prepared by drop-casting 80 μL of PEDOT:PSS solution onto a glass substrate and spreading evenly. The deposited film was dried in air at 50 °C for 1 h and then kept at 140 °C for another 10 min. For the post-treatment, initially, 100 μL formamide was dropped on the PEDOT:PSS film, kept overnight at 25 °C, rinsed thrice with deionized water, and then annealed again at 140 °C for 10 min. These initial post-treated samples were cooled before further treatment with 2 M ionic liquids diluted in methanol. For this, 100 μL of ionic liquid solution was dropped onto a formamide-treated PEDOT:PSS film at room temperature, left overnight, rinsed thrice with deionized water, and finally annealed at 140 °C for thermoelectric characterization. Free-standing formamide- and ionic liquid-treated PEDOT:PSS films can be made to fall off from the glass substrates by immersing them in deionized water. The folded and crumpled free-standing films can be straightened using ethanol drops, which flatten the hybrid films owing to the creation of a surface tension gradient and the Marangoni effect. Then, these free-standing films (thickness of ~2 μm and a size of 10 × 10 cm^2) can be transferred onto a hot plate and dried at 60 °C for use in a thermoelectric generator assembly.

This journal is © The Royal Society of Chemistry 2022

J. Mater. Chem. A, 2022, **10**, 18792–18802 | **18793**

Thermoelectric characterization

The thermoelectric parameters of the films, including electrical conductivity and the Seebeck coefficient, were measured under a helium atmosphere in the in-plane direction (parallel to the sample surface). The testing sample size was 15 mm × 5 mm, sliced from a square piece with dimensions of 15 mm × 15 mm. Silver paste was used to coat both ends of the samples. The measurement was performed in the temperature range of approximately 313–423 K using a commercially available ZEM-3 system (ADAVANCE RIKO, Inc). At each temperature, the conductivity is measured by the dc four-terminal method at thermal equilibrium. The Seebeck coefficient is measured by detecting the temperature difference with the thermocouple probes pressed against the same side of the sample, followed by the measurement of thermal electromotive force between the same wires. Three different data points were noted at each temperature, and the Seebeck coefficient was calculated by finding the linearly fitted slope.

Fabrication and measurements of thermoelectric generators

The free-standing modified PEDOT:PSS films were cut into rectangular thermopile pieces with identical sizes of 25 mm length and 4.5 mm width. Seven pieces were placed on the polyethylene terephthalate (PET) substrate based on the series–parallel connection design in the thermoelectric generators and electrically connected by using silver paste. For fabricating a proof-of-concept wearable device, an ionic liquid-modified PEDOT:PSS thermopile was further placed into an ethylene-vinyl acetate (EVA) foam substrate with combined copper wires/silver paste as connections; one half was exposed to the ambient air and the other half was buried under the foam substrate to directly make contact with the skin. The electrical power generation capability of the thermoelectric generator was evaluated using a custom-built measurement system under dark ambient conditions. The temperature differences were induced in the thermoelectric generator using two sheets of the Peltier device. The thermocouple temperature monitoring of the sample surfaces during environmental testing was performed using a Keithley DAQ 6510 multimeter system. It should be noted that the temperature difference of the wearable device was estimated from the difference between the human skin and ambient temperatures. The current and corresponding voltages across the two electrodes on the sample were measured by using a Keithley 2450 source meter and Keithley 2182A nanovoltmeter, respectively.

3.   Results and discussion

First, ionic liquid-modulated PEDOT:PSS was synthesized by readily adding ionic liquid into pristine PEDOT:PSS aqueous solution. Four ionic liquid salts with various alkyl chain lengths in cations were used as additives in PEDOT:PSS, including 1,3-dimethylimidazolium (MMIM), 1-ethyl-3-methylimidazolium (EMIM), 1-butyl-3-methylimidazolium (BMIM), and 1-hexyl-3-methyl-imidazolium (HMIM) cations with tetrafluoroborate (BF_4) anions, denoted as MMIM BF_4, EMIM BF_4, BMIM BF_4, and

HMIM BF_4, respectively. These four ionic liquids have the commonality of providing stable cations and BF_4 anions (see Fig. 1). Ionic liquids exhibit favorable water-solvating properties as well as possess high thermal stabilities[56] and act as non-volatile plasticizers. They can be mixed with PEDOT:PSS to formulate hybrid thermoelectric aqueous ink. The ionic interactions and exchange among the ionic liquids and PEDOT:PSS contribute to the structural rearrangement of PEDOT. Simultaneous changes are observed in the oxidation state resulting from the introduction of secondary doping agents, where the cations and BF_4 anions in ionic liquids are electrostatically coupled with positively charged conducting PEDOT and negatively charged insulating PSS, respectively. The physical properties of the four ionic liquids summarized in Table S2† can be tuned by modifying the alkyl chain lengths of the cationic components. Naturally, the ionic liquids with shorter alkyl chains of cations exhibit lower viscosity and better aqueous solubility; thus, more homogeneous PEDOT:PSS/MMIM BF_4 hybrid films can be produced by the spin-coating process, as demonstrated in Fig. S1.†

A comparison between the in-plane thermoelectric properties of all the PEDOT:PSS/XMIM BF4 (1%) hybrid films after performing the DMSO post-treatment is shown in Fig. 2. The temperature-dependent thermoelectric parameters of all the PEDOT:PSS/XMIM BF4 samples were characterized in the range of 313–423 K, where the electrical conductivity decreased and the Seebeck coefficient increased with temperature.[57] These variations can be associated with the increase in carrier scattering due to lattice vibrations as the temperature increases, resulting in the metal/semiconductor-like characteristics of PEDOT:PSS/XMIM BF4 hybrid films. All the PEDOT:PSS/ionic liquids films exhibit enhanced conductivity (~40–80 fold) as compared with the pristine PEDOT:PSS. The maximum conductivity at 313 K is 433.8, 532.7, 679.3, and 804.4 S cm^{-1} for PEDOT:PSS hybrid films modified by MMIM BF_4, EMIM BF_4, BMIM BF_4, and HMIM BF_4, respectively; these values are comparable to the previously achieved values.[41,42,58,59] Meanwhile, the obtained positive Seebeck coefficients of the modified films range from 22.4 to 26.0 μV K^{-1} at 313 K, compared to 17.2 μV K^{-1} for the pristine PEDOT:PSS film measured under the same conditions. Fig. 2(b) shows a clear improvement in the Seebeck coefficient, reaching 28.7–35.7 μV K^{-1} at a higher temperature of 423 K. Consequently, it is also clear that the
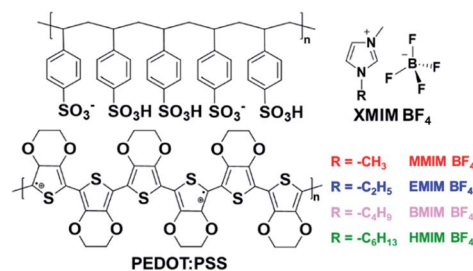

Fig. 1 A schematic of the chemical structures of PEDOT:PSS and XMIM BF$_4$ ionic liquids with various cationic species (X = M (methyl), E (ethyl), B (butyl), and H (hexyl)).

18794 | J. Mater. Chem. A, 2022, 10, 18792–18802

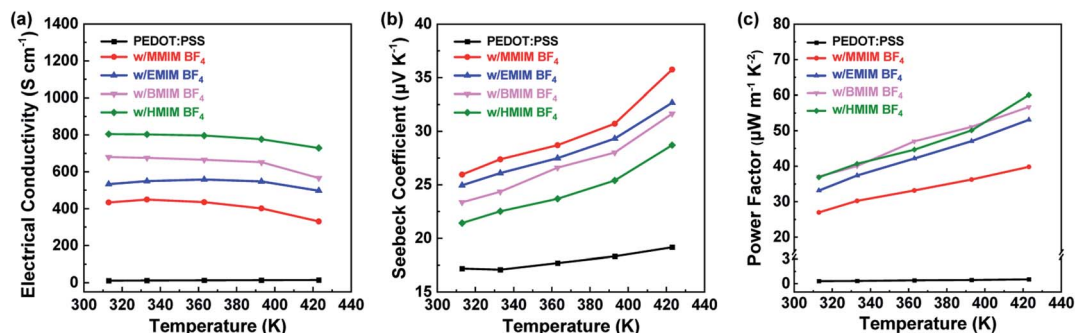This journal is © The Royal Society of Chemistry 2022

Fig. 2 Temperature-dependent (a) electrical conductivity, (b) Seebeck coefficient, and (c) power factor of the spin-coated pristine PEDOT:PSS and PEDOT:PSS/XMIM BF$_4$ (1%) hybrid films with DMSO post-treatment. It is noted that PEDOT:PSS mixed with MMIM BF$_4$, EMIM BF$_4$, BMIM BF$_4$, and HMIM BF$_4$ is denoted as w/MMIM BF$_4$, w/EMIM BF$_4$, w/BMIM BF$_4$, and w/HMIM BF$_4$ respectively.

presence of ionic liquids with small-sized cations on the PEDOT:PSS modification leads to a higher Seebeck coefficient but lower conductivity. Owing to the intercoupling phenomenon between the electrical conductivity and the Seebeck coefficient, an optimized power factor of 39.8, 53.1, 56.7, and 60.1 μV m^{-1} K^{-2} (shown in Fig. 2(c)) is obtained for the PEDOT:PSS film modified with MMIM BF$_4$, EMIM BF$_4$, BMIM BF$_4$, and HMIM BF$_4$, respectively. The thermoelectric properties of PEDOT:PSS/XMIM BF4 hybrid films without DMSO post-treatment were also investigated (Fig. S2†). Obviously, the increased electrical conductivity without a reduction in the Seebeck coefficient can be obtained with the help of the secondary DSMO doping process.[32]

Despite the reduction in the conductivity, films modified with MMIM BF$_4$ display a higher Seebeck coefficient. Besides, a non-homogeneous gel-like mixture was obtained when a higher concentration of other larger-sized cations in ionic liquids was added into the PEDOT:PSS solution. Therefore, the doping efficiency of PEDOT:PSS/ionic liquid hybrid films was further investigated by the extra- or less-MMIM BF$_4$ solution modification process. The three additional compositions of hybrid solutions, that is, 0.5%, 1.5%, and 2% of MMIM BF$_4$ in a PEDOT:PSS dispersion, were prepared as target samples, where the homogenous distribution of the MMIM BF$_4$ within PEDOT:PSS could be observed at a higher concentration. Fig. 3(a) shows a comparison of the MMIM BF$_4$ content-dependent thermoelectric properties (measured at 313 K) of hybrid films after DMSO post-treatment. With an increase in the MMIM BF$_4$ content, the corresponding conductivity of the hybrid films decreases, showing the highest conductivity of 777.2 S cm^{-1} for 0.5% MMIM BF$_4$. Concurrently, the Seebeck coefficient increases gradually with increasing content of MMIM BF$_4$, with a maximum value of 34.5 μV K^{-1} at 3 wt%. The optimized power factor compromised between conductivity and the Seebeck coefficient reaches 43.9 μW m^{-1} K^{-2} for the 1.5 wt% MMIM BF4-modified PEDOT:PSS film. It is well known that organic polar solvents can significantly increase the conductivity of PEDOT:PSS films, resulting in a screening effect between the positively charged PEDOT chains and negatively charged PSS chains, thus lowering their coulombic interactions.[60] Here, the extremely high dielectric constant ($\varepsilon = 109$) of

formamide was used during the post-treatment to further improve the conductivity of the hybrid films.[61] The temperature-dependent thermoelectric performance of 1.5 wt% MMIM BF4-modified PEDOT:PSS films with formamide post-treatment was measured (Fig. 3(b)). As expected, the conductivity increases up to ~850 S cm^{-1} at 313–423 K, while the Seebeck coefficient (~25.4 μV K^{-1}) drops slightly as compared to that of the hybrid film with DMSO post-treatment at 313 K. Correspondingly, the champion samples based on the 1.5 wt% MMIM BF4-modified PEDOT:PSS film with formamide post-treatment exhibit a much higher power factor of 54.1 and 75.0 μV m^{-1} K^{-2} at 313 and 423 K, respectively.
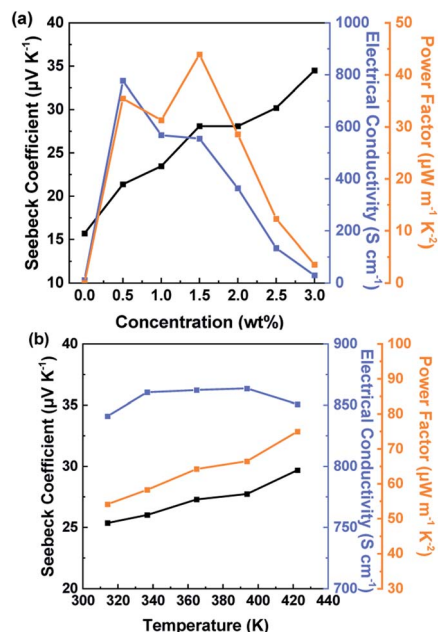

Fig. 3 (a) Electrical conductivity, Seebeck coefficient, and power factor of spin-coated PEDOT:PSS/MMIM BF$_4$ hybrid films after DMSO post-treatment as a function of MMIM BF$_4$ content (wt%). (b) Temperature-dependent conductivity, Seebeck coefficient, and power factor of PEDOT:PSS/MMIM BF$_4$ (1.5%) hybrid films with formamide post-treatment.

PEDOT:PSS/XMIM BF4 hybrid films with various cation sizes in ionic liquids were further studied through various characterization techniques, including UV-vis-NIR spectroscopy, Raman spectroscopy, X-ray photoelectron spectroscopy (XPS), and grazing incidence wide angle X-ray scattering (GIWAXS), to further understand the mechanism of the enhanced thermoelectric properties. The reaction between XMIM BF4 and PEDOT:PSS within the hybrid films results in a change in the resonance and doping level of PEDOT chains, which can be evidenced by the absorption transitions of the neutron, polaronic, and bipolaronic states in the UV-vis-NIR spectra (Fig. 4(a)). The absorption spectra associated with the majority of pristine PEDOT:PSS indicate a highly doped state, as demonstrated by the appearance of a broad band at the longer wavelengths of >1200 nm originating from the presence of the bipolaron species and accompanied by a minor absorption near 900 nm from the polaron species.[62] The presence of the XMIM BF4 ionic liquid compounds in modified PEDOT:PSS resulting in the loss of the bipolaron band is consistent with the results of previous studies,[41,42] where the polaron absorption band is distinctly observed. This indicates that XMIM BF4 contributes to the conversion of bipolaron to polaron species in the PEDOT:PSS film, which is triggered by the reduction in the oxidation level/dedoping of the PEDOT:PSS film. In addition, decreasing the alkyl chain length of the cation in XMIM BF4, especially for MMIM BF$_4$, results in a relatively higher concentration of polarons from the most significant dedoping of polarons. A partial dedoping to the neutral state and absorption within 500–700 nm associated with a π–π* transition of the PEDOT chains is also observed. The electrical conductivity of PEDOT is proportional to the oxidation/p-doping level, while the Seebeck coefficient is correlated with the population of the polaron state.[63] Thus, the conductivity reduces in the order of PEDOT:PSS/HMIM BF$_4$, PEDOT:PSS/BMIM BF$_4$, PEDOT:PSS/ EMIM BF$_4$, and PEDOT:PSS/MMIM BF$_4$, in conjunction with the reverse trend for the Seebeck coefficient. Overall, MMIM BF$_4$ results in a large increase in the polaronic transition compared to other ionic liquids, implying that MMIM BF$_4$ acts as a more effective reducing agent due to the stronger activity of the short

alkyl chain in the MMIM$^+$ cation. This observation is supported by the larger Seebeck coefficient observed in the MMIM BF$_4$-modified PEDOT:PSS film. Additionally, Raman spectroscopy of the XMIM BF$_4$-modified PEDOT:PSS films (see Fig. 4(b)) was conducted to reveal information on the conformational changes in the PEDOT chains. A complex series of peaks from 1350 to 1600 cm^{-1} with a characteristic band at 1435 cm^{-1} was observed for the pristine PEDOT:PSS film, which is consistent with the results of a previous study[64] addressing the $C_\alpha = C_\beta$ symmetrical stretching vibration of the five-member ring. It should be noted that there is no shift in this peak between the pristine PEDOT:PSS film and one with formamide post-treatment (Fig. S3†).[61] We observed a redshift and narrowing of the width of this band for PEDOT:PSS with ionic liquids: from 1435 cm^{-1} to 1429 cm^{-1} (MMIM BF$_4$), 1431 cm^{-1} (EMIM BF$_4$), 1432 cm^{-1} (BMIM BF$_4$), and 1434 cm^{-1} (HMIM BF$_4$). The shift is similar to that observed after the modification of PEDOT:PSS films by typical reductants,[65,66] indicating a change from a predominately benzoid structure (coil confirmation) to a quinoid structure (mixed linear-coil conformation) in the PEDOT:PSS chain.[65,67] This increased planarity from the ionic liquid modification may contribute to a more efficient charge delocalization and a concomitant improvement in conductivity compared to that of the pristine PEDOT:PSS film. Therefore, the shift in this vibration mode for modified XMIM BF$_4$, in the order of MMIM BF$_4$ > EMIM BF$_4$ > BMIM BF$_4$ > HMIM BF$_4$, shows the same change trend in the doping level based on the dedoping process from the bipolaron to the polaron/neutral state, giving the highest Seebeck coefficient and compromised electrical conductivity for the MMIM BF$_4$-modified PEDOT:PSS film.

Next, the possible interaction of ionic liquids with PEDOT:PSS thin films was investigated by XPS analysis. The characteristic S 2p peaks of XMIM BF$_4$-modified PEDOT:PSS films were deconvoluted into high binding energies between 166 and 172 eV and low binding energies between 162 and 166 eV assigned to sulfonate sulfur in PSS and thiophene sulfur in PEDOT,[68] respectively, as shown in Fig. 5. Table S3† summarizes the deconvoluted components of the S 2p XPS spectra, which can be used to determine the atomic ratios of PEDOT to PSS estimated by using the integration of the peak area. It can be seen that the sulfur atom ratio of PEDOT to PSS changes from pristine PEDOT : PSS (1 : 2.44) to HMIM BF$_4$ (1 : 1.35), BMIM BF$_4$ (1 : 1.26), EMIM BF$_4$ (1 : 1.23), and MMIM BF$_4$ (1 : 1.16), since the ionic liquid modification significantly removes the insulating PSS layer. This analysis indicates that the shorter the alkyl chain length in the cation species of XMIM BF$_4$, the better the removal of PSS; ~52% of PSS chains are removed by the addition of MMIM BF$_4$. The correlation between the degree of counter ion exchange and the microstructural transformation in the mixture of PEDOT:PSS and XMIM BF$_4$ was studied by grazing-incidence wide angle X-ray scattering (GIWAXS). Fig. 6(a–e) presents the typical 2D scattering patterns of GIWAXS, and Fig. 6(f) shows the linear offset of 1D GIWAXS in the horizontal direction associated with mixed edge-on/face-on oriented PEDOT molecules. The inner and outer scattering rings in the 2D pattern of the pristine PEDOT:PSSS film, corresponding to the peaks at $q_{xy} = 1.20$ Å^{-1} and 1.76 Å^{-1}, depend
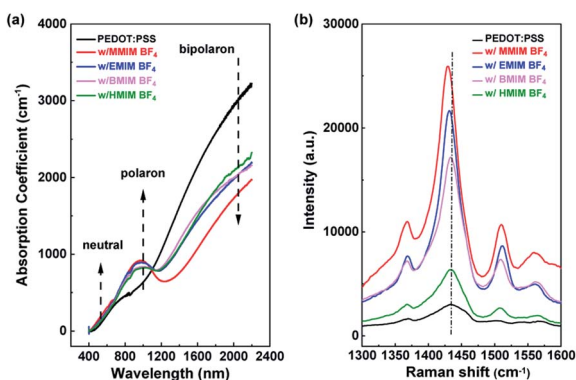

Fig. 4 (a) UV-vis-NIR spectra and (b) Raman spectra of the spin-coated pristine PEDOT:PSS and PEDOT:PSS/XMIM BF$_4$ (1.5%) hybrid films with formamide post-treatment.
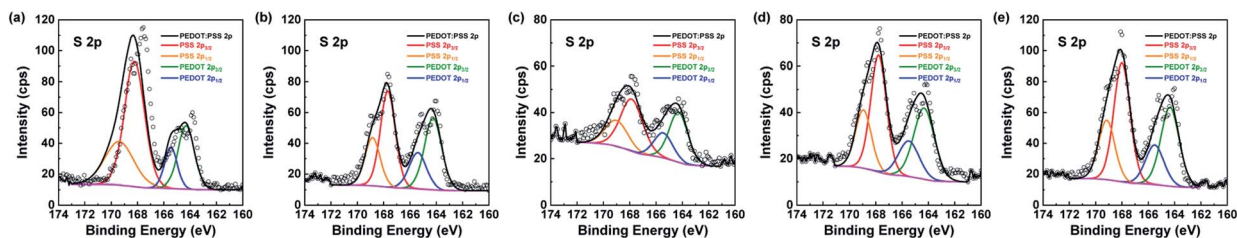
18796 | J. Mater. Chem. A, 2022, 10, 18792–18802

This journal is © The Royal Society of Chemistry 2022

Fig. 5 XPS S 2p core level spectra SS of the spin-coated (a) pristine PEDOT:PSS films and (b) PEDOT:PSS/MMIM BF$_4$, (c) PEDOT:PSS/EMIM BF$_4$, (d) PEDOT:PSS/BMIM BF$_4$, and (e) PEDOT:PSS/HMIM BF$_4$ hybrid films with formamide post-treatment.

on (100) stacked PSS and (010) stacked PEDOT molecules, respectively.[69] Another characteristic peak at $q_{xy} = 0.23$ Å^{-1} is attributed to the (100) PEDOT crystal plane. The peak at $q_{xy} = 1.76$ Å^{-1} indicates a d-spacing of 3.57 Å in the π–π stacking direction for the pristine PEDOT:PSS film. When the films are deposited from a PEDOT:PSS dispersion containing XMIM BF$_4$, the peak shifts to a higher q_{xy} value, accompanied by a shorter π–π distance for densely packed PEDOT crystallites, which may contribute to efficient charge transport along the π–π stacking direction.[70] Besides, the XMIM BF$_4$-modified PEDOT:PSS films exhibit a significant reduction in the diffraction intensity, which indicates the loss of some PSS chains from the PEDOT:PSS films. This higher PEDOT fraction in the crystals suggests the predominantly oriented PEDOT crystallites in the modified PEDOT:PSS films, which contribute to the improved thermoelectric performance.[71] Additionally, the new peak corresponding to the (200) crystal plane of PEDOT can be observed at $q_{xy} = 0.50$ Å^{-1}, which indicates the enhanced crystalline ordering upon the addition of XMIM BF$_4$. Moreover, the enhancement in conductivity induced by ionic liquid mixing agrees with the change in the aggregation state as observed from the AFM images (Fig. S4†). When ionic liquids are added to PEDOT:PSS, the bright region (assigned to PEDOT) expands into the PSS domain and becomes more interconnected in the overall area.[72] The PEDOT:PSS/XMIM BF$_4$ hybrid films yield a larger surface root-mean-square roughness (R_{rms}), from 1.68 nm (pristine) to 1.72, 1.89, 2.06, and 2.20 nm for MMIM BF$_4$, EMIM BF$_4$, BMIM BF$_4$, and HMIM BF$_4$ modification, respectively, which is rationalized by the increased fraction of PEDOT-rich grains and the removal of the PSS chains.

The interpretations from observing the physical/chemical properties of PEDOT:PSS/XMIM BF$_4$ hybrid films are consistent. The doping level of the PEDOT:PSS films can be manipulated by mixing with varying-alkyl-chain-length cation species of XMIM BF$_4$; thus, both conductivity and the Seebeck coefficient can be simultaneously enhanced in these PEDOT:PSS/XMIM BF$_4$ hybrid films. The addition of ionic liquids with good charge diffusivity can help the ionic exchange reaction between XMIM$^+$:BF$_4^-$ and PEDOT$^+$:PSS$^-$ through electrostatic interaction. Therefore, the selective separation of insulating PSS$^-$ from the PEDOT$^+$ chains contributes to the coil-to-linearly extended PEDOT conformation for achieving the conducting channel, which confirms the remarkably enhanced conductivity upon the addition of all XMIM BF$_4$ ionic liquids. This hypothesis is supported by XPS (Fig. 5) and GIWAXS (Fig. 6) quantification as

well as the more modest 700-fold enhancement in computed charge carrier mobility obtained by Hall measurement (Fig. S5†). Besides, the modification of PEDOT:PSS induced by XMIM BF$_4$ results in an increase in the polaron density and a decrease in the oxidation level, suggesting an enhanced Seebeck coefficient. As compared with pristine PEDOT:PSS, the higher number of diffuse cations from the shortest alkyl chain length (in the case of MMIM BF$_4$) is able to significantly increase the Seebeck coefficient (by a factor of ~1.9) owing to the low viscosity of MMIM BF$_4$ among all the ionic liquids. The enhanced Seebeck coefficient with the addition of XMIM BF$_4$ additives is also driven by the variations in the relative charge carrier concentration (Fig. S5†). A heavily doped pristine PEDOT:PSS film has a carrier density of 2.1×10^{21} cm^{-3}, whereas the charge concentration caused by the dedoping of the PEDOT:PSS film with XMIM BF$_4$ is reduced by approximately one order of magnitude (~10^{20} cm^{-3}). The lowest charge
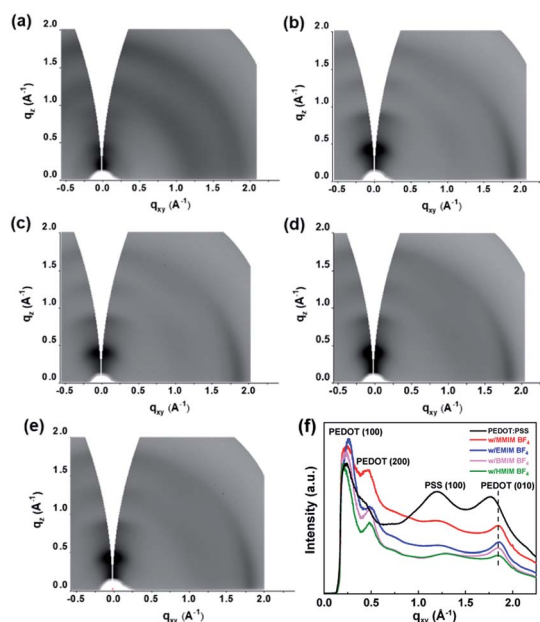

Fig. 6 2D GIWAXS patterns of spin-coated (a) pristine PEDOT:PSS films and (b) PEDOT:PSS/MMIM BF$_4$, (c) PEDOT:PSS/EMIM BF$_4$, (d) PEDOT:PSS/BMIM BF$_4$, and (e) PEDOT:PSS/HMIM BF$_4$ hybrid films with formamide post-treatment. (f) 1D in-plane line-cuts of pristine PEDOT:PSS and PEDOT:PSS/XMIM BF$_4$ hybrid films with formamide post-treatment.

This journal is © The Royal Society of Chemistry 2022

J. Mater. Chem. A, 2022, **10**, 18792–18802 | **18797**

concentration of 1.2×10^{20} cm^{-3} from the smallest cations in MMIM BF$_4$ is indeed coincident with the most reducing/dedoping capability, which also confirms the highest Seebeck coefficient. The variation in the electronic structure of PEDOT:PSS films influenced by the interaction with MMIM BF$_4$ was also investigated by photoelectron spectroscopy in air (PESA), as shown in Fig. S6.† The work function of the pristine PEDOT:PSS film is -5.13 eV and shifts upward to -4.71, -4.76, -4.87, and -4.90 eV with the addition of MMIM BF$_4$, EMIM BF$_4$, BMIM BF$_4$, and HMIM BF$_4$, respectively, indicating that MMIM BF$_4$ induces the most reducing reaction and the highest Seebeck coefficient.[41,43,73] However, the most efficient ionic liquids pair in enhanced conductivity from the longer alkyl chain in the cation species (in the case of HMIM BF$_4$) due to the lower binding energy between XMIM and BF$_4$ (ref. 74 and 75) guarantees a more favorable ion exchange with PEDOT:PSS, which screens their interaction with the doped PEDOT domains. As a result, the conductivity of the PEDOT:PSS films treated with ionic liquids monotonically decreases in the order of HMIM BF$_4$ > BMIM BF$_4$ > EMIM BF$_4$ > MMIM BF$_4$; the binding energy increases as the alkyl chain length of the cation decreases. Meanwhile, a strong dedoping process from MMIM BF$_4$ enables a decrease in conductivity because the charge concentration decreases as the mobilities change slightly. It can be concluded that MMIM BF$_4$ dedopes the PEDOT chains most significantly, which results in the highest Seebeck coefficient and the lowest conductivity at a low oxidation level. However, the Seebeck coefficient enhancement cannot compensate for the conductivity loss and a slightly reduced PF value is obtained.

From the comprehensive analysis above, it can be seen that the resistivity of the spin-coated thermoelectric films is high, which significantly affects their conductivity and becomes the bottleneck for limiting the power output of thermoelectric generators. Conversely, the hybrid solution becomes viscous after directly introducing the ionic liquid additive. Moreover, the rough and aggregated film surfaces fabricated by spin-coating lead to many defects, which impede the charge carrier transport with their mediate high conductivity. In addition, the 100 nm thin films are not mechanically strong enough, and it may be difficult to achieve stable and flexible thermoelectric devices using these films. Therefore, thick film-based PEDOT:PSS (on the micrometer scale) are fabricated by the drop-casting method followed by sequential treatment with formamide and 1.5% XMIM BF$_4$ in methanol; their thermoelectric performances are given in Fig. 7. Similar to the results of spin-coated PEDOT:PSS films, the conductivity increases from 1447.3 S cm^{-1} to 1534.1, 1654.2, and 1974.2 S cm^{-1} for MMIM BF$_4$, EMIM BF$_4$, BMIM BF$_4$, and HMIM BF$_4$, respectively, as the alkyl chain length of the cationic species in XMIM BF$_4$ increases, whereas the Seebeck coefficient decreases from 24.4 μV K^{-1} to 21.4, 19.6, and 19.5 μV K^{-1} at 313 K. This could be attributed to the significant dedoping effect of the PEDOT:PSS film treated with MMIM BF$_4$. However, a decrease in the Seebeck coefficient for a drop-cast, thicker hybrid film compared to that for a spin-coated thinner one can be observed. This could be attributed to the fact that the post-treatment of the PEDOT:PSS with XMIM BF$_4$ is not as effective as directly mixing

PEDOT:PSS and XMIM BF$_4$. Owing to the significant increase in conductivity from the thick film, the PEDOT:PSS film deposited by drop-casting and after MMIM BF$_4$ post-treatment performs the best, yielding a moderate-high conductivity (1447.3 S cm^{-1}), high Seebeck coefficient (24.4 μV K^{-1}), and power factor (86.2 μW m^{-1} K^{-2}). Table S1† compares the thermoelectric properties of recently reported PEDOT:PSS composites post-treated with ionic liquids, and Fig. S7† shows the Seebeck coefficient and power factor as a function of conductivity. It is apparent that the electrical conductivity in our films is relatively high, although the Seebeck coefficient is not impressive. We need to emphasize that our thermoelectric measurement is under a low-pressure helium atmosphere. According to the previous report regarding the ionic Seebeck effect in conducting polymers,[76] the ionic Seebeck coefficient is detected only at high relative humidity, which indicates that pure electronic conductors can dominate our measured Seebeck coefficient. The reported high Seebeck coefficient may involve combined ionic and electric rearrangement in the thermal gradient due to the measurement under ambient conditions.

To verify the potential applications of the ionic liquid-modified PEDOT:PSS films, a wearable thermoelectric generator is assembled, and the human body is used as the heat source. However, good film quality and a sufficiently thick conducting polymer thermoelectric film printed on any target substrate surface are the key parameters. Inspired by recent work, Xie *et al.* proposed the strategy of creating Marangoni force to help unfold the crumpled thick polymer films and perform transfer printing on various surfaces.[77] In the transfer printing method, the drop-cast PEDOT:PSS/MMIM BF$_4$ thick films were suspended in deionized water, and the Marangoni force produced from the surface tension gradient by adding alcohol into the water pulled the films on the water surface. Thus, the free-standing PEDOT:PSS/MMIM BF$_4$ films can transfer onto various surfaces such as the non-flat back of the hand (Fig. 8(a)). When drying was done in a large ambient area, free-standing PEDOT:PSS/MMIM BF$_4$ films (demonstrated in 10 × 10 cm^2;
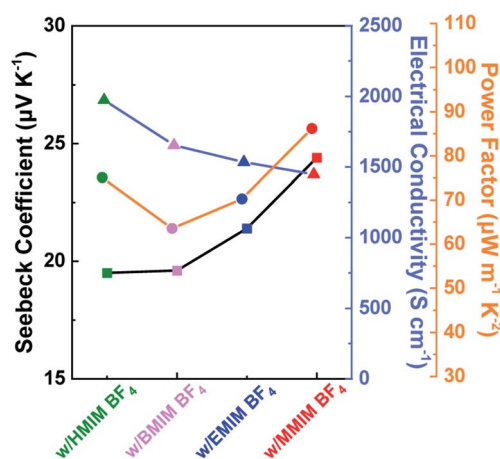

Fig. 7 Electrical conductivity, Seebeck coefficient, and power factor of the drop-cast PEDOT:PSS film after sequential post-treatment with formamide and ionic liquids.
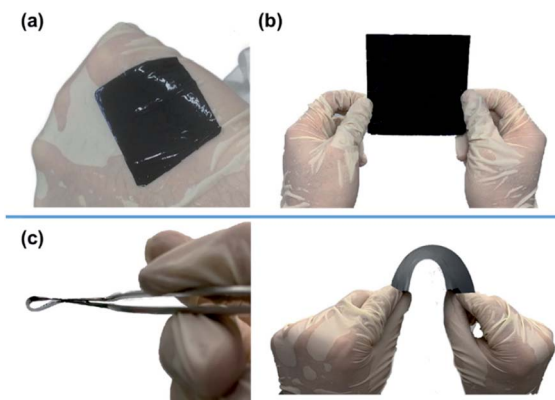
Fig. 8 Photos of (a) the PEDOT:PSS/MMIM BF$_4$ hybrid film attached conformally to the back of the human hand, (b) the free-standing PEDOT:PSS/MMIM BF$_4$ hybrid film in a large area, and (c) its flexibility demonstration.

Fig. 8(b)) with good flexibility could be obtained (Fig. 8(c)). These free-standing films were cut into several suitable rectangular pieces (25 mm × 4.5 mm), and seven legs of tailored thermoelectric films were designed and connected by silver paste contacts (inset of Fig. S8†). The prototype of a thermoelectric generator was supported by a PET substrate, with a total resistance of ~124 Ω. The mechanical endurance of the device was assessed by bending tests with a curvature radius of 3 mm. The change in the circuit resistance of the module under repeated bending up to 500 cycles is less than 5%, as shown in Fig. S8(a).† Thus, the thermoelectric generator shows remarkable mechanical robustness, making reassembly into various conformal structures possible. Moreover, the unencapsulated device shows good environmental stability (humidity and temperature were maintained near 40% and 25 ± 3 °C),

resulting in an average resistance increase of ~10% after storing for 28 days (Fig. S8(b)†). To obtain the accurate temperature applied on the thermoelectric generator, a temperature-controlling apparatus was connected to the Peltier module to adjust the temperature on the heating plate, where the thermocouples were used to detect the exact temperature difference between two electrodes on both ends of the test specimens. Through characterization of the thermoelectric output performance of the thermoelectric generator, the operating voltage and the corresponding power outputs as functions of electrical current of the module were plotted under varying temperature gradients of 5.7, 8.4, 11.3, and 14.0 K (Fig. 9(a)). The output voltage is negatively linear to the increasing current density but proportionally increases with the increasing temperature gradient due to the increased Seebeck coefficient, achieving the highest open-circuit thermovoltage of 2.4 mV at a temperature gradient of 14.0 K. The ideal computed thermovoltage (ΔV) from the thermoelectric generator can be estimated from the relationship: $\Delta V = nS \times \Delta T$, where n and S are the total number (7) and Seebeck coefficient (24.4 μV K^{-1} at 313 K) of PEDOT:PSS thermoelectric strips, respectively, and ΔT is the temperature difference between the hot and cold sides. The experimentally obtained ΔV is close to the calculated value (~2.39 mV). The low disparity between these two values is probably due to the slight heat loss at the thermal contact, indicating the efficiency of serially connected MMIM BF$_4$-modified PEDOT:PSS thermoelectric strips for the module. Correspondingly, when the temperature difference increases from 5.7 to 14.0 K, the module shows a quadratic increase in the output power, as shown in Fig. 9(a). The maximum output power density, which is calculated from the thermal-gradient-generated power divided by the total area of the device module (7 pieces × 25 mm × 4.5 mm), is 10.4 nW for a temperature difference of 14.0 K. The module performance of other related
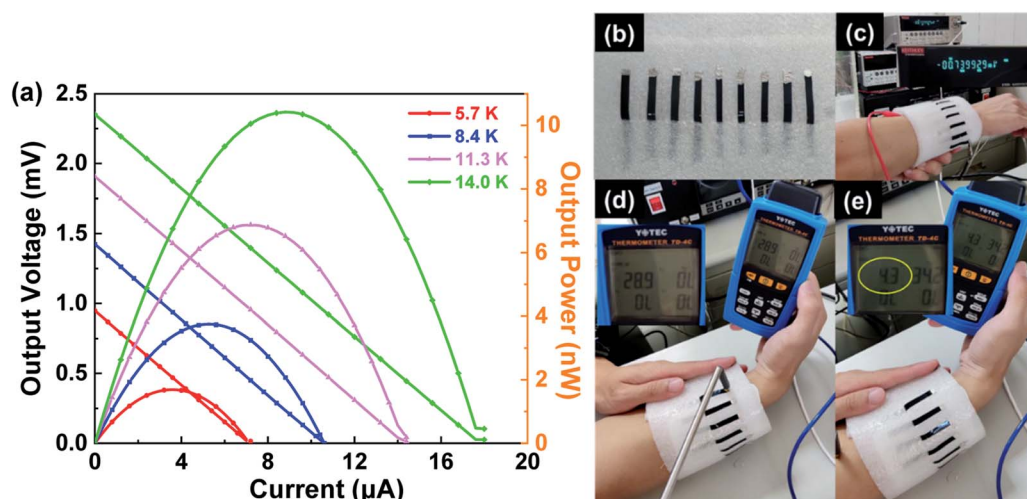

Fig. 9 (a) Output thermovoltage (open symbols) and power (closed symbols) as a function of current of the 7-leg flexible thermoelectric generator at various temperature differences. (b) Photograph of the 9-leg wearable thermoelectric generator module, where the strips are interspersed inside and outside of the foam and connected with silver paste and copper wire. (c) Demonstration of the wearable thermoelectric generator module worn on the curved surface of the human wrist; a thermovoltage of 0.74 mV is generated due to the temperature difference between the (d) ambient and (e) human skin surface.

This journal is © The Royal Society of Chemistry 2022

J. Mater. Chem. A, 2022, **10**, 18792–18802 | **18799**

PEDOT:PSS-based thermoelectric generators is compared, as listed in Table S4.† These results demonstrate that our prototype module made from PEDOT:PSS/MMIM BF$_4$ hybrid films generates a moderate-high thermoelectric voltage and power from low-grade heat due to the optimized conductivity and Seebeck coefficient.

To verify realistic applications, the 9-leg wearable thermoelectric generator with optimized thermoelectric properties described above was assembled onto an ethylene-vinyl acetate (EVA) foam substrate and worn on the human lower arm as a heat source, as shown in Fig. 9(b). One side of the module closely adheres with the arm and the other side is exposed to the ambient atmosphere (Fig. 9(c)). Both the arm skin temperature and ambient temperature are recorded using thermocouples; there is a 4.3 K temperature difference between the ambient temperature (28.9 K; Fig. 9(d)) and the skin surface temperature (34.2 K; Fig. 9(e)). The obtained thermovoltage of ∼0.74 mV (Fig. 9(c)) suggests that the $\Delta V/\Delta T$ value per leg in the module is 19.1 μV K^{-1}. Considering the above-mentioned Seebeck coefficient of 24.4 μV K^{-1} for the free-standing PEDOT:PSS/MMIM BF$_4$ film measured at 313 K, the slight reduction can be attributed to the decrease in the Seebeck coefficient of each leg with decreasing temperature during the experiment. To further strengthen the mechanical stability and self-recovery, our free-standing composites can be potentially blended with thermoplastic polymer binders such as polyurethane[78] and polyvinyl alcohol[79,80] for stretchable thermoelectric devices.

4. Conclusions

In summary, the influence of the cation size in ionic liquid (XMIM BF$_4$) additives for PEDOT:PSS hybrid films was systematically studied to elucidate the mechanism of enhanced thermoelectric properties. The thermoelectric results reveal that both conductivity and the Seebeck coefficient can be significantly increased upon the addition of ionic liquids to the blend solution. The small-sized cations in the ionic liquid result in PEDOT:PSS hybrid films with the highest Seebeck coefficient of 24.4 μV K^{-1} owing to the decrease in the oxidation level from more diffuse cations of less viscous MMIM BF$_4$, which is evidenced by the dedoping process in the UV-vis results and the lowest charge concentration value from Hall measurement. In contrast, the highest conductivity achieved upon modification with HMIM BF$_4$ results from the favorable ion exchange with PEDOT:PSS and the lesser extent of dedoping of HMIM BF$_4$. The changes in the thermoelectric properties can be rationally linked with the cation size in ionic liquids. Finally, the free-standing PEDOT:PSS film post-treated with MMIM BF$_4$ was sliced and assembled into a thermoelectric module with the assistance of the Marangoni force. The device module was fabricated with a peak output power of 10.4 nW at a temperature difference of 14.0 K. As a demonstration of the module for practical application, a prototype of a wearable thermoelectric generator from the 9-leg MMIM BF$_4$-treated PEDOT:PSS film on the EVA foam substrate exhibited a thermovoltage of ∼0.74 mV with the lower human arm acting as a heat source (temperature difference of 4.3 K).

Conflicts of interest

There are no conflicts to declare.

Notes and references

1 G. J. Tan, L. D. Zhao and M. G. Kanatzidis, *Chem. Rev.*, 2016, **116**, 12123–12149.

2 E. S. Toberer, A. F. May and G. J. Snyder, *Chem. Mater.*, 2010, **22**, 624–634.

3 L. Yang, Z. G. Chen, M. S. Dargusch and J. Zou, *Adv. Energy Mater.*, 2018, **8**, 1701797.

4 X. L. Shi, J. Zou and Z. G. Chen, *Chem. Rev.*, 2020, **120**, 7399–7515.

5 J. He and T. M. Tritt, *Science*, 2017, **357**, eaak9997.

6 R. Kroon, D. A. Mengistie, D. Kiefer, J. Hynynen, J. D. Ryan, L. Y. Yu and C. Muller, *Chem. Soc. Rev.*, 2016, **45**, 6147–6164.

7 S. Masoumi, S. O'Shaughnessy and A. Pakdel, *Nano Energy*, 2022, **92**, 106774.

8 M. Lindorf, K. A. Mazzio, J. Pflaum, K. Nielsch, W. Brutting and M. Albrecht, *J. Mater. Chem. A*, 2020, **8**, 7495–7507.

9 G. Prunet, F. Pawula, G. Fleury, E. Cloutet, A. J. Robinson, G. Hadziioannou and A. Pakdel, *Mater. Today Phys.*, 2021, **18**, 100402.

10 H. Wang and C. Yu, *Joule*, 2019, **3**, 53–80.

11 Y. Lu, J. Y. Wang and J. Pei, *Chem. Mater.*, 2019, **31**, 6412–6423.

12 H. Y. Yao, Z. Fan, H. L. Cheng, X. Guan, C. Wang, K. Sun and J. Y. Ouyang, *Macromol. Rapid Commun.*, 2018, **39**, 1700727.

13 M. Bharti, A. Singh, S. Samanta and D. K. Aswal, *Prog. Mater. Sci.*, 2018, **93**, 270–310.

14 I. Petsagkourakis, K. Tybrandt, X. Crispin, I. Ohkubo, N. Satoh and T. Mori, *Sci. Technol. Adv. Mater.*, 2018, **19**, 836–862.

15 G. M. Chen, W. Xu and D. B. Zhu, *J. Mater. Chem. C*, 2017, **5**, 4350–4360.

16 B. Russ, A. Glaudell, J. J. Urban, M. L. Chabinyc and R. A. Segalman, *Nat. Rev. Mater.*, 2016, **1**, 16050.

17 L. Deng and G. Chen, *Nano Energy*, 2021, **80**, 105448.

18 W. R. Zhao, J. M. Ding, Y. Zou, C. A. Di and D. B. Zhu, *Chem. Soc. Rev.*, 2020, **49**, 7210–7228.

19 T. L. D. Tam and J. W. Xu, *J. Mater. Chem. A*, 2021, **9**, 5149–5163.

20 J. T. Li and T. Lei, *Chem.–Asian J.*, 2021, **16**, 1508–1518.

21 M. X. Zeng, D. Zavanelli, J. H. Chen, M. Saeidi-Javash, Y. P. Du, S. LeBlanc, G. J. Snyder and Y. L. Zhang, *Chem. Soc. Rev.*, 2022, **51**, 485–512.

18800 | *J. Mater. Chem. A*, 2022, **10**, 18792–18802

This journal is © The Royal Society of Chemistry 2022

22 Y. Tian and F. Molina-Lopez, *Nanoscale*, 2021, **13**, 5202–5215.

23 Y. F. Xue, C. M. Gao, L. R. Liang, X. Wang and G. M. Chen, *J. Mater. Chem. A*, 2018, **6**, 22381–22390.

24 S. N. Patel and M. L. Chabinyc, *J. Appl. Polym. Sci.*, 2017, **134**, 44403.

25 H. J. Song, Q. F. Meng, Y. Lu and K. F. Cai, *Adv. Electron. Mater.*, 2019, **5**, 1800822.

26 Z. Fan and J. Y. Ouyang, *Adv. Electron. Mater.*, 2019, **5**, 1800769.

27 Y. Zheng, H. N. Zeng, Q. Zhu and J. W. Xu, *J. Mater. Chem. C*, 2018, **6**, 8858–8873.

28 S. Panigrahy and B. Kandasubramanian, *Eur. Polym. J.*, 2020, **132**, 109726.

29 I. Petsagkourakis, N. Kim, K. Tybrandt, I. Zozoulenko and X. Crispin, *Adv. Electron. Mater.*, 2019, **5**, 1800918.

30 Y. Yang, H. Deng and Q. Fu, *Mater. Chem. Front.*, 2020, **4**, 3130–3152.

31 J. S. Yun, S. Choi and S. H. Im, *Carbon Energy*, 2021, **3**, 667–708.

32 J. J. Luo, D. Billep, T. Blaudeck, E. Sheremet, R. D. Rodriguez, D. R. T. Zahn, M. Toader, M. Hietschold, T. Otto and T. Gessner, *J. Appl. Phys.*, 2014, **115**, 054908.

33 D. A. Mengistie, C.-H. Chen, K. M. Boopathi, F. W. Pranoto, L.-J. Li and C.-W. Chu, *ACS Appl. Mater. Interfaces*, 2015, **7**, 94–100.

34 Z. Fan, D. Du, Z. Yu, P. Li, Y. Xia and J. Ouyang, *ACS Appl. Mater. Interfaces*, 2016, **8**, 23204–23211.

35 S. R. S. Kumar, N. Kurra and H. N. Alshareef, *J. Mater. Chem. C*, 2016, **4**, 215–221.

36 O. Bubnova, Z. U. Khan, A. Malti, S. Braun, M. Fahlman, M. Berggren and X. Crispin, *Nat. Mater.*, 2011, **10**, 429–433.

37 G. H. Kim, L. Shao, K. Zhang and K. P. Pipe, *Nat. Mater.*, 2013, **12**, 719–723.

38 O. Bubnova, M. Berggren and X. Crispin, *J. Am. Chem. Soc.*, 2012, **134**, 16456–16459.

39 D. Zhao, A. Wurger and X. Crispin, *J. Energy Chem.*, 2021, **61**, 88–103.

40 C. Liu, J. Xu, B. Lu, R. Yue and F. Kong, *J. Electron. Mater.*, 2012, **41**, 639–645.

41 S. Kee, H. Kim, S. H. K. Paleti, A. El Labban, M. Neophytou, A.-H. Emwas, H. N. Alshareef and D. Baran, *Chem. Mater.*, 2019, **31**, 3519–3526.

42 N. Saxena, B. Pretzl, X. Lamprecht, L. Bießmann, D. Yang, N. Li, C. Bilko, S. Bernstorff and P. Müller-Buschbaum, *ACS Appl. Mater. Interfaces*, 2019, **11**, 8060–8071.

43 T. A. Yemata, Y. Zheng, A. K. K. Kyaw, X. Wang, J. Song, W. S. Chin and J. Xu, *Front. Chem.*, 2020, **7**, 870.

44 Z. Fan, D. Du, X. Guan and J. Ouyang, *Nano Energy*, 2018, **51**, 481–488.

45 J. J. Luo, D. Billep, T. Waechtler, T. Otto, M. Toader, O. Gordan, E. Sheremet, J. Martin, M. Hietschold, D. R. T. Zahnd and T. Gessner, *J. Mater. Chem. A*, 2013, **1**, 7576–7583.

46 N. Kim, S. Lienemann, I. Petsagkourakis, D. A. Mengistie, S. Kee, T. Ederth, V. Gueskine, P. Leclere, R. Lazzaroni, X. Crispin and K. Tybrandt, *Nat. Commun.*, 2020, **11**, 1424.

47 Y. N. Lu, A. Y. Wu, C. W. Sha, X. C. Hang and D. J. Young, *Chem.–Asian J.*, 2021, **16**, 2740–2744.

48 Q. K. Li, M. J. Deng, S. M. Zhang, D. K. Zhao, Q. L. Jiang, C. F. Guo, Q. Zhou and W. S. Liu, *J. Mater. Chem. C*, 2019, **7**, 4374–4381.

49 T. A. Yemata, Y. Zheng, A. K. K. Kyaw, X. Z. Wang, J. Song, W. S. Chin and J. W. Xu, *Mater. Adv.*, 2020, **1**, 3233–3242.

50 A. Mazaheripour, S. Majumdar, D. Hanemann-Rawlings, E. M. Thomas, C. McGuiness, L. d'Alencon, M. L. Chabinyc and R. A. Segalman, *Chem. Mater.*, 2018, **30**, 4816–4822.

51 J. Atoyo, M. R. Burton, J. McGettrick and M. J. Carnie, *Polymers*, 2020, **12**, 559.

52 M. Z. Du, X. Y. Chen and K. Zhang, *ACS Appl. Energy Mater.*, 2021, **4**, 4070–4080.

53 X. Li, R. K. Zou, Z. Liu, J. Mata, B. Storer, Y. Chen, W. H. Qi, Z. K. Zhou and P. Zhang, *npj Flex. Electron.*, 2022, **6**, 6.

54 X. L. Y. J. J. Z. Jiaji Yang and J. Qinglin, *Chin. Phys. B*, 2022, **31**, 027302.

55 Q. Li, Q. Zhou, W. Xu, L. Wen, J. Li, B. Deng, J. Zhang, H. Xu and W. Liu, *ACS Appl. Mater. Interfaces*, 2022, **14**, 27911–27921.

56 M. Armand, F. Endres, D. R. MacFarlane, H. Ohno and B. Scrosati, *Nat. Mater.*, 2009, **8**, 621–629.

57 V. Karthikeyan, J. U. Surjadi, J. C. K. Wong, V. Kannan, K.-H. Lam, X. Chen, Y. Lu and V. A. L. Roy, *J. Power Sources*, 2020, **455**, 227983.

58 A. Mazaheripour, S. Majumdar, D. Hanemann-Rawlings, E. M. Thomas, C. McGuiness, L. d'Alencon, M. L. Chabinyc and R. A. Segalman, *Chem. Mater.*, 2018, **30**, 4816–4822.

59 X. Li, Z. Liu, Z. Zhou, H. Gao, G. Liang, D. Rauber, C. W. M. Kay and P. Zhang, *ACS Appl. Polym. Mater.*, 2021, **3**, 98–103.

60 N. A. A. Shahrim, Z. Ahmad, A. Wong Azman, Y. Fachmi Buys and N. Sarifuddin, *Mater. Adv.*, 2021, **2**, 7118–7138.

61 A. K. K. Kyaw, T. A. Yemata, X. Wang, S. L. Lim, W. S. Chin, K. Hippalgaonkar and J. Xu, *Macromol. Mater. Eng.*, 2018, **303**, 1700429.

62 J. C. Gustafsson, B. Liedberg and O. Inganäs, *Solid State Ionics*, 1994, **69**, 145–152.

63 O. Bubnova, Z. U. Khan, H. Wang, S. Braun, D. R. Evans, M. Fabretto, P. Hojati-Talemi, D. Dagnelund, J.-B. Arlin, Y. H. Geerts, S. Desbief, D. W. Breiby, J. W. Andreasen, R. Lazzaroni, W. M. Chen, I. Zozoulenko, M. Fahlman, P. J. Murphy, M. Berggren and X. Crispin, *Nat. Mater.*, 2014, **13**, 190–194.

64 A. Lenz, H. Kariis, A. Pohl, P. Persson and L. Ojamäe, *Chem. Phys.*, 2011, **384**, 44–51.

65 S. Garreau, G. Louarn, J. P. Buisson, G. Froyer and S. Lefrant, *Macromolecules*, 1999, **32**, 6807–6812.

66 M. Stavytska-Barba and A. M. Kelley, *J. Phys. Chem. C*, 2010, **114**, 6822–6830.

67 M. Łapkowski and A. Proń, *Synth. Met.*, 2000, **110**, 79–83.

68 D. A. Mengistie, M. A. Ibrahem, P.-C. Wang and C.-W. Chu, *ACS Appl. Mater. Interfaces*, 2014, **6**, 2292–2299.

69 S. Kee, N. Kim, B. S. Kim, S. Park, Y. H. Jang, S. H. Lee, J. Kim, J. Kim, S. Kwon and K. Lee, *Adv. Mater.*, 2016, **28**, 8625–8631.

This journal is © The Royal Society of Chemistry 2022

J. Mater. Chem. A, 2022, **10**, 18792–18802 | **18801**

70 H. Sirringhaus, P. J. Brown, R. H. Friend, M. M. Nielsen, K. Bechgaard, B. M. W. Langeveld-Voss, A. J. H. Spiering, R. A. J. Janssen, E. W. Meijer, P. Herwig and D. M. de Leeuw, *Nature*, 1999, **401**, 685–688.

71 D. K. Taggart, Y. Yang, S.-C. Kung, T. M. McIntire and R. M. Penner, *Nano Lett.*, 2011, **11**, 125–131.

72 C. Badre, L. Marquant, A. M. Alsayed and L. A. Hough, *Adv. Funct. Mater.*, 2012, **22**, 2723–2727.

73 X. Hu, K. Zhang, J. Zhang, S. Wang and Y. Qiu, *ACS Appl. Energy Mater.*, 2018, **1**, 4883–4890.

74 A. de Izarra, S. Park, J. Lee, Y. Lansac and Y. H. Jang, *J. Am. Chem. Soc.*, 2018, **140**, 5375–5384.

75 P. Nanthanasit, N. Chattrapiban, M. Jitvisate, P. Nimmanpipug and S. Rimjaem, *J. Phys.: Conf. Ser.*, 2021, **1719**, 012023.

76 H. Wang, U. Ail, R. Gabrielsson, M. Berggren and X. Crispin, *Adv. Energy Mater.*, 2015, **5**, 1500044.

77 C. Xie, W. Wang, C. Li, Q. Nie, L. Sun, W. Zeng, F. Qin, T. Liu, X. Dong, H. Han, H. Fang, D. Zhao and Y. Zhou, *Adv. Mater. Technol.*, 2021, **6**, 2100181.

78 X. He, Y. Hao, M. He, X. Qin, L. Wang and J. Yu, *ACS Appl. Mater. Interfaces*, 2021, **13**, 60498–60507.

79 S. Xu, Z. Fan, S. Yang, X. Zuo, Y. Guo, H. Chen and L. Pan, *ACS Sens.*, 2021, **6**, 1120–1128.

80 Z. Li, L. Deng, H. Lv, L. Liang, W. Deng, Y. Zhang and G. Chen, *Adv. Funct. Mater.*, 2021, **31**, 2104836.

18802 | *J. Mater. Chem. A*, 2022, **10**, 18792–18802

This journal is © The Royal Society of Chemistry 2022